Draft version March 31, 2016
Preprint typeset using LaTeX style emulateapj v. 04/17/13

arXiv:1603.09109v1 [astro-ph.HE] 30 Mar 2016

THE MULTI-WAVELENGTH CHARACTERISTICS OF THE TEV BINARY LS I +61°303

L. Saha[1], V. R. Chitnis, A. Shukla[2], A. R. Rao and B. S. Acharya
Tata Institute of Fundamental Research, Homi Bhabha Road, Colaba, Mumbai 400 005, India
Draft version March 31, 2016

ABSTRACT

We study the characteristics of the TeV binary LS I +61°303 in radio, soft X-ray, hard X-ray, and gamma-ray (GeV and TeV) energies. The long term variability characteristics are examined as a function of the phase of the binary period of 26.496 days as well as the phase of the super orbital period of 1626 days, dividing the observations into a matrix of 10×10 phases of these two periods. It is found that the long term variability can be described by a sine function of the super orbital period, with the phase and amplitude systematically varying with the binary period phase. We also find a definite wavelength dependent change in this variability description. To understand the radiation mechanism, we define three states in the orbital/ super orbital phase matrix and examine the wide band spectral energy distribution. The derived source parameters indicate that the emission geometry is dominated by a jet structure showing a systematic variation with the orbital/ super orbital period. We suggest that LS I +61°303 is likely to be a micro-quasar with a steady jet.

Subject headings: radiation mechanisms: non-thermal – stars: individual (LS I +61°303) – X-rays: binaries – gamma rays: general – stars: emission-line, Be

1. INTRODUCTION

LS I +61°303, a Galactic high-mass X-ray binary system located at a distance of 2 kpc (Frail & Hjellming 1991), is detected in the energy range from radio to γ-rays exhibiting strong variable emission. It consists of a B0 main-sequence star with a circumstellar disk (i.e a Be star) and a compact object of unknown nature. The orbital period of the system is estimated to be P_{orb} = 26.496 days and it also exhibits a long term periodic variation with a superorbital period of P_{sup} = 1667 days (Gregory 2002; Massi & Jaron 2013; Massi et al. 2015). However, very recently the superorbital period is estimated to be 1626 days using 37 years of radio data (Massi & Torricelli-Ciamponi 2016). The zero orbital phase corresponds to $T_{0,orb} = 2443366.775 + nP_{orb}\ JD$. According to the most recent radial velocity measurements, the orbit is elliptical with eccentricity of e = 0.537 ± 0.034 and periastron passage occurring around phase $\phi = 0.275$, apastron passage at $\phi = 0.775$, superior conjunction at $\phi = 0.081$, and inferior conjunction at ϕ = 0.313 (Aragona et al. 2009).

High angular resolution VLBI radio data has shown the presence of high-energy particle outflow possibly related to jet-like ejection on the time scale of a orbital period (Paredes et al. 1998; Massi et al. 2004). However, the observed morphological changes in the data collected at different epochs reported by Dhawan et al. (2006) support a scenario of binary pulsar. Recent detailed VLBA radio images, obtained by reprocessing same data-set, through the orbital period established the presence of one sided and double sided radio structures supporting a precessing microquasar model (Massi et al. 2012).

labsaha@ncac.torun.pl, vchitnis@tifr.res.in
[1] Present address : Nicolaus Copernicus Astronomical Center, Torun, Poland
[2] Present address : ETH Zurich, Institute for Particle Physics, Otto-Stern-Weg 5, 8093 Zurich, Switzerland

Long-term monitoring of the source during 2007-2011 by Proportional Counter Array (PCA) onboard Rossi X-ray Timing Explorer (RXTE) established the superorbital modulation in X-rays and a shift of superorbital phase by 0.2 between radio and X-ray data (Li et al. 2012; Chernyakova et al. 2012). Very recently, superorbital modulation at MeV–GeV γ-rays in the apastron phase (0.5 –1.0) has been established by Fermi-LAT (Ackermann et al. 2013) based on the data taken during 2008 August 4 to 2013 March 24.

This source has often shown complex behaviour in very high energy γ-rays. LS I +61°303 was first observed at TeV energies by the MAGIC telescope system during 2005 October – 2006 March with a significance of 8.7σ in the orbital phase 0.4–0.7, establishing it as a γ-ray binary (Albert et al. 2006). The VERITAS observations carried out during 2006 September – 2007 February confirmed TeV emission from this source (Acciari et al. 2008). However, further observations of the source by both MAGIC and VERITAS have shown different flux levels (Acciari et al. 2011; Aleksic et al. 2012; Aliu et al. 2013). These observations at TeV energies show that the source behaves differently in different orbital cycles suggesting a variable nature of the source. Variability of the source almost in all wavelengths could possibly be related to superorbital modulation of the fluxes, which has been shown at radio, X-ray and MeV–GeV γ-rays detected by Fermi-LAT (Gregory 2002; Li et al. 2012; Chernyakova et al. 2012; Ackermann et al. 2013). Hence long term multiwaveband study of this source can provide an important observational support for unveiling the nature of the source and the emission mechanisms.

With this motivation, we have studied the radio, X-ray and γ-ray data from this source collected over a period longer than the superorbital period. We have studied the variation of flux as a function of orbital and superorbital phases. We have also studied multiwaveband Spectral Energy Distribution (SED) of the source in some of the

phases. This paper is organized as follows: In section 2, the data set used for these studies and analysis procedure is described. Variation of the flux with the orbital and the superorbital phases is discussed in section 3. The SEDs and their interpretation in terms of microquasar model are given in section 4 followed by a discussion and conclusions in section 5.

2. MULTIWAVEBAND DATA AND ANALYSIS

In the last few years, LS I +61°303 has been observed extensively by various instruments. In the present work, we have used data from radio, X-ray and γ-ray bands. Radio data used here is from Richards et al. (2011) and Massi et al. (2015). These are 15 GHz observations from 40 m single-dish telescope at Owens Valley Radio Observatory (OVRO). Data on LS I +61°303 were collected during MJD 54908.8 – 56795.0 (2009 March – 2014 May). Observations were carried out approximately twice a week.

X-ray data were obtained from PCA onboard RXTE and X-ray Telescope or XRT onboard Swift. The PCA is an array of five identical Xenon filled proportional counter units (PCUs) (Bradt et al. 1993) covering an energy range from 2 to 60 keV with a total collecting area of 6500 cm^2. Data were collected over the period MJD 50143 – 55924 and standard analysis procedure was used to generate PCA light curves over the energy range of 2 – 9 keV.

The XRT onboard Swift consists of a grazing incidence Wolter I telescope which focuses X-rays on a CCD (Burrows et al. 2005). This instrument has an effective area of 110 cm^2, 23.6 arcmin field of view (FOV) and 15 arcsec resolution (half-power diameter). It covers an energy range of 0.2 to 10 keV. Swift-XRT light curves were obtained from the site [3]. Data is collected over the period of MJD 53980 – 57039 (2006 September 2 – 2015 January 17). Details of the procedure used for generating these light curves is given in Evans et al. (2007).

High energy γ-ray data are obtained from Large Area Telescope (LAT) onboard Fermi. The Fermi-LAT is a pair production telescope (Atwood et al. 2009) covering energy range of 20 MeV to 300 GeV with a FOV of $\geq$ 2.5 sr. The data taken over the period MJD 54682.9 – 57145.9 (2008 August 4 – 2015 May 3) were analysed in the present work. Circular region of interest (ROI) with radius 15° centred at the position of RA(J2000) = 02^h 40^m 34^s and Dec(J2000) = 61° 15′ 25″ was used for extracting the data. Fermi Science Tools (FST-v10r0p5) with event class Pass 8 data were used for Galactic point source analysis. Since the Earth's limb is a strong source of background γ-rays, they were filtered out with a zenith-angle cut of 100°. A python based software tool *enrico* (Sanchez & Deil 2013) was used to do standard binned likelihood analysis. The γ-ray events in the data were binned in 8 logarithmic bins in the energies between 300 MeV and 300 GeV. Since the point-spread function (PSF) of LAT is large, the sources from outside of the ROI may contribute at low energies affecting true estimates of the fluxes for the sources considered in this analysis. In order to account for this, exposure map was expanded by another 10° outside the ROI, for all events, as suggested by Abdo et al. (2009).

[3] *http://www.swift.ac.uk/user_objects/*

We studied the spectral properties of the γ-ray emission by comparing the observational results with the models of the sources present in the ROI. To get the best-fit model parameters, the spatial distribution and spectral models of the sources are convolved with the instrument response function (IRF) and exposure of the observation. In this work, we used newly introduced IRF version *P8R2_SOURCE_V6*. There are 85 point-like sources and some diffuse background sources from the 3rd Fermi-LAT catalog located in the ROI. In order to account for the emission from background sources, we considered two component background model: diffuse Galactic emission (gll_iem_v06.fits) and isotropic emission component (iso_P8R2_SOURCE_V6_v06.txt) consisting of emission from extra galactic background, unresolved sources and instrumental background.

The binned likelihood analysis was used for both background and source modelling using *gtlike* tool of FST. Spectral parameters for the source outside the 3° region centred at the LS I +61°303 position were kept fixed. However, parameters except normalization for the point-like background sources were fixed or varied based on their strength and distance from the center of the ROI. Light curve was generated over the energy range of 300 MeV – 300 GeV.

For Very High Energy (VHE) or TeV band, published data collected during 2005-2011 from MAGIC (Albert et al. 2009) and VERITAS (Acciari et al. 2008, 2011; Aliu et al. 2013) experiments are used. These are the ground based atmospheric Cherenkov experiments located in La Plama and Arizona, respectively.

3. MULTIWAVEBAND FLUX VARIATION

In order to study the variation of flux as a function of orbital and superorbital phases, datasets from various wavebands were folded in 10 superorbital phase bins using the ephemeris given by Massi & Torricelli-Ciamponi (2016). Each of these bins correspond to 163 days. Further, in each phase bin, 10 orbital phase bins were generated. Average flux was estimated in each of these 10 × 10 phase bins. X-ray fluxes from Swift-XRT and RXTE-PCA in 10 × 10 orbital vs superorbital bins are shown in the top left and the top right panels of Fig. 1, respectively. These panels show a definite pattern in the variation of flux over the orbital and the superorbital phases for both XRT and PCA data. It can be seen from the figure that the source is bright in the orbital phase range $\sim$ 0.4 – 0.8 while the corresponding superorbital phase is at $\sim$ 0.3 – 0.8. The highest flux in each of the orbital cycles shifts towards apastron passage as the superorbital phase value increases. Similar plots generated for the γ-ray data from Fermi-LAT and 15 GHz radio data from OVRO are given in the middle panels of Fig. 1. As noted by earlier studies, there is a definite shift in the pattern for the radio data: the maximum flux is at the same orbital phase range (0.4 – 0.8) as in the X-ray data, but the super orbital phase range is shifted to 0.7 to 1.4. The Fermi-LAT data shows some indication of enhanced emission in the orbital phase 0.4 to 0.8, but unlike the other wavebands, the enhancements in the super orbital phases are not very clear. Plots for VHE γ-ray data from VERITAS and MAGIC are shown in bottom panels of Fig. 1. But the data-set is not extensive enough to detect any trend in this case.

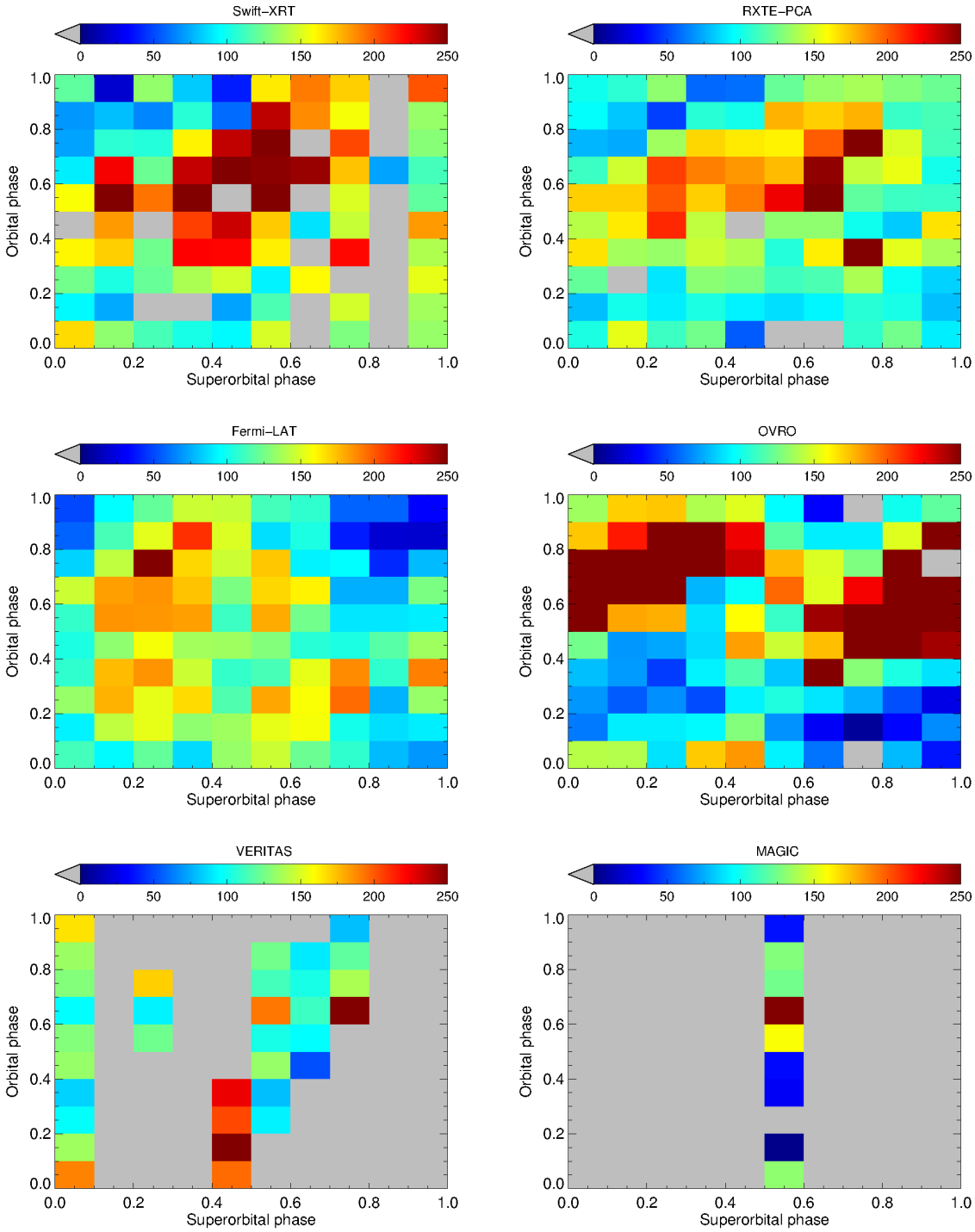

FIG. 1.— Multiwaveband flux as a function of orbital and superorbital phases. Top panels show X-ray flux from XRT data in the left panel and PCA data in the right panel. Middle left panel corresponds to γ-ray data from Fermi-LAT and middle right panel shows radio data from OVRO. Bottom panels correspond to VHE γ-ray flux from VERITAS (left panel) and MAGIC (right panel). Flux values in each panel are normalized setting median flux to 125, i.e. the middle of the scale.

To investigate this aspect further, variation of the flux as a function of superorbital phase was studied in various orbital phase bins. Variation of the X-ray count rates from Swift-XRT with superorbital phase is shown in the top left panel of Fig. 2. Similar plots for RXTE-PCA, Fermi-LAT and OVRO are shown in the top right, bottom left and bottom right panels of the same figure, respectively. In each panel, different curves from bottom to top correspond to orbital phases 0-0.1, 0.1-0.2, .. , 0.9-1.0. Curves are shifted with respect to each other for the sake of clarity. Error bars correspond to the standard deviation in each bin. To parameterize this variation, data are fitted with a constant and alternatively with a sine function of the form $f(t) = f_o + A \times sin(\phi_s - \phi_o)$, where f_o, A and ϕ_o are model parameters and ϕ_s is the superorbital phase. Sine function with a period of 1626 days gives a better fit than the constant. It can be seen from the figure that there is a definite shift in the superorbital phase for the peak flux with respect to the orbital phase. Phase at the peak of the function, peak function value and the ratio of the maximum to the minimum function values are listed in Table 1. Results are given only for the cases where modulation is seen clearly in Fig. 2. Fig. 3 shows these results graphically, where superorbital phase for peak of the function value is plotted as a function of orbital phase bins for XRT, PCA, Fermi-LAT and OVRO data. This figure clearly shows the trend of increasing superorbital phase for peak as a function of orbital phase near apastron. The wavelength dependent phase difference between superorbital phase for given orbital phase bin is also evident. This difference remains more or less constant in various orbital phase bins near apastron.

4. SPECTRAL ENERGY DISTRIBUTION

We have investigated the spectral properties of the source at different orbital and superorbital phases. Following Figure 1 three different regions were chosen. Two of the regions are bright in most of the wavebands and the third one is of low brightness. These regions are i) Super orbital phase: 0.3 – 0.5 Orbital phase: 0.6 – 0.8, ii) Super orbital phase: 0.5 – 0.7 Orbital phase: 0.6 – 0.8 and iii) Super orbital phase: 0.0 – 0.2 Orbital phase, 0.0 – 0.2 (hereafter state1, state2, and state3, respectively). X-ray and Fermi-LAT spectral data were analysed for these three regions. Fermi-LAT analysis procedure is already described in section 2. We have analysed spectral data from Swift-XRT and RXTE-PCA corresponding to the states mentioned above. Some details of these observations are given in Table 2. Dates for XRT and PCA observations for each of the three states are listed in the table along with the total observation duration.

In case of XRT we have fitted spectrum over the energy range of 0.3 to 10 keV. Source and background photons were selected using the tool XSELECT. Data were recorded in Photon Counting (PC) mode for these observations. Source photons were selected from a circular region with the radius of 20 pixels (i.e. 47 arcseconds), whereas nearby circular region with radius of 40 pixels was used for extracting background photons. Events with grades 0-12 were selected in this analysis. The spectral data were rebinned using tool GRPPHA with 20 photons per bin. Standard response matrices and ancillary response files were used.

In case of PCA, standard 2 data with time resolution of 16 s and 128 channels of energy information were used. Data were analysed using HEASOFT (version 6.15). For each observation, data were filtered using the standard procedure given in the RXTE Cook Book. The tool 'pcabackest' was used for generation of background model, calibration files for 'faint' source (less than 40 ct/sec/PCU) from RXTE GOF were used. To improve statistics, only data from top layer of PCU2 was used.

A combined spectral fit was performed for XRT and PCA data. The PCA spectrum was normalized with the XRT spectrum for this purpose. The XRT and PCA spectra covering the energy range of 0.7-20 keV were fitted by using XSPEC with a powerlaw with the line-of-sight absorption, which was kept free during the fit. Model parameters for the combined fit as well as for only XRT data are listed in Table 3. Since the bandwidth of the data is quite limited, we find a correlation between the power-law index and the absorption, indicating that a steeper power-law is compensated by a large absorption. For the wide band fitting, we use the joint XRT-PCA fit because the higher energy data from PCA constrains the power-law better.

Fermi-LAT SEDs for the three states fitted with a cut-off powerlaw are given in Fig. 4 and model parameters are listed in Table 4. Some differences are seen in the spectral indices for γ-rays between state1 and other states (see Table 4). In case of X-ray data some steepening of the spectrum is seen as flux decreases, as indicated by variation in spectral index (see Table 3).

We have investigated the spectral energy distributions (SEDs) of the source. The state3 does not have TeV data and hence we have made a detailed SED study for the other two states. These states are bright in all wavebands and hence can be used as a template to understand the emission mechanisms. VERITAS spectral data obtained from Acciari et al. (2011) corresponds to state1. For radio flux, the average of 15 GHz data from OVRO described in section 2 is used. This sets an upper limit on the modelled radio flux. In addition, we have also plotted radio data from Strickman et al. (1998), which correspond to orbital phase of 0.8 and superorbital phase of 0.8.

Since LS I +61°303 is identified as a potential microquasar based on radio observations, high energy emission is likely to be produced in jets. In case of microquasars, compact object could be a neutron star or a black hole accreting matter from a companion star which presumably drives relativistic outflow or jet from the compact object. Acceleration of charged particles in the jet produces high energy emission. We have considered this scenario to model the SEDs. In the context of leptonic model, the low energy emission arises from Synchrotron emission from ultra-relativistic electrons in the jet. Whereas the high energy emission arises from inverse Compton scattering of soft photons, which could be either soft photons from Synchrotron radiation (Synchrotron Self-Compton or SSC model) or photons from companion star or accretion disk (External Compton model). In this work, relativistic jet making an angle of 30° (Gupta & Bottcher (2006) and reference therein) with our line of sight is considered. Electrons are assumed to have a broken power-law energy spectrum given by

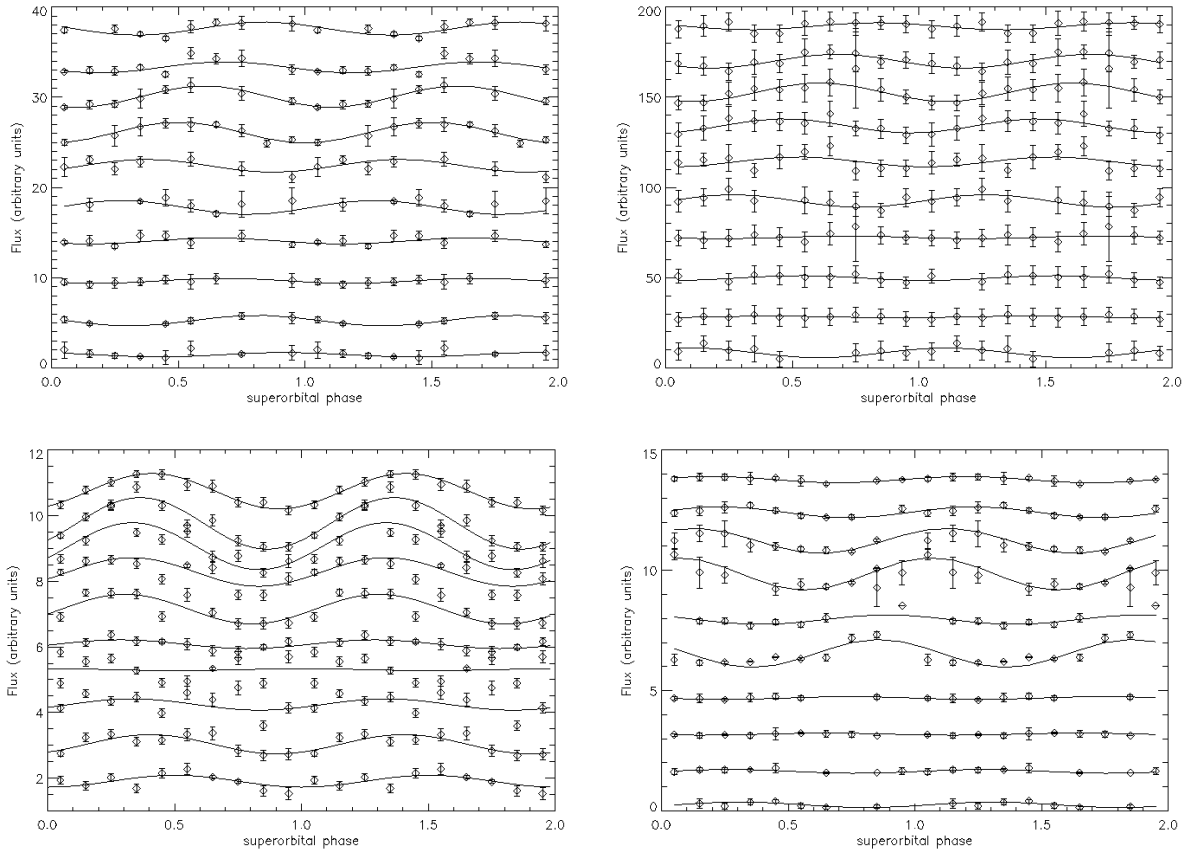

FIG. 2.— Variation of flux with superorbital phase for XRT (top left), PCA (top right), Fermi-LAT (bottom left) and OVRO (bottom right). In each panel curves from bottom to top correspond to orbital phases 0-0.1, 0.1-0.2, .. , 0.9-1.0. These curves are shifted along Y-axis for the sake of clarity.

TABLE 1
PEAK FLUX AND CORRESPONDING SUPERORBITAL (SO) PHASE FROM SINE FUNCTION FIT IN VARIOUS ORBITAL PHASE BINS

Orbital Phase	XRT SO phase at peak	XRT peak flux ($10^{-1}ph$ cm^{-2} s^{-1})	XRT ratio max /min)	PCA SO phase at peak	PCA peak flux ($10^{-1}ph$ cm^{-2} s^{-1})	PCA ratio max /min)	Fermi-LAT SO phase at peak	Fermi-LAT peak flux ($10^{-1}ph$ cm^{-2} s^{-1})	Fermi-LAT ratio max /min)	OVRO SO phase at peak	OVRO peak flux ($10^{-1}ph$ cm^{-2} s^{-1})	OVRO ratio max /min)
0.0–0.1	-	-	-	-	-	-	-	-	-	0.30	4.19	23.88
0.1–0.2	-	-	-	-	-	-	-	-	-	0.26	2.22	3.25
0.2–0.3	-	-	-	-	-	-	-	-	-	0.58	2.32	1.86
0.3–0.4	-	-	-	-	-	-	-	-	-	0.70	2.51	2.01
0.4–0.5	0.28	2.79	3.16	0.26	1.60	1.80	0.28	2.21	1.13	0.80	8.73	7.75
0.5–0.6	0.38	3.12	1.86	0.54	1.83	1.68	0.30	2.60	1.53	0.90	6.50	2.58
0.6–0.7	0.50	3.26	3.55	0.46	1.75	1.70	0.34	2.71	1.47	0.06	9.31	3.10
0.7–0.8	0.60	3.27	3.79	0.62	1.64	2.12	0.34	2.78	2.06	0.10	9.93	2.85
0.8–0.9	0.60	2.53	3.19	0.66	1.46	2.50	0.36	2.54	2.60	0.30	6.41	6.91
0.9–1.0	0.84	2.34	2.71	0.78	1.16	1.51	0.42	2.28	1.89	0.26	3.82	1.82

$$\frac{dn_e}{d\gamma} \propto \begin{cases} \gamma^{-\alpha} \text{ for } \gamma < \gamma_{br} \\ \gamma^{-\beta} \exp\left(-\frac{\gamma}{\gamma_c}\right) \text{ for } \gamma_{br} \leq \gamma \leq \gamma_c \end{cases}$$

where, n_e denotes the number density of the electrons, γ is the Lorentz factor of the electron, α and β are spectral indices, γ_{br} break energy and γ_c the highest energy of the electron.

For this source, the distance is taken as 2 kpc (Hutchings & Crampton 1981; Frail & Hjellming 1991) and Lorentz factor for bulk motion is assumed to be 1.25 (Massi et al. 2004). The models are shown for state1 and state2 respectively in Figure 5 and Figure 6.

Here it is assumed that the radio, X-ray and γ-ray emissions originate in the same region and the magnetic field in emission blob is quite high, of the order of 10^3 G. Rest of the model parameters are fitted and these parameters are listed in Table 5. To explain the TeV γ-ray emission it was necessary to include IC of photons

TABLE 2
Observation log for XRT and PCA

State	Instrument	Observation dates	Number of observations	Total duration seconds
1 Superorb. phase : 0.3–0.5 Orbital phase : 0.6–0.8	XRT	2010-10-22, 2010-11-18, 2010-12-17, 2014-10-18, 2014-10-20 - 2014-10-23, 2014-11-14, 2014-11-15, 2014-12-11 - 2014-12-13	13	15805
	PCA	2010-02-25, 2010-02-28, 2010-03-24, 2010-03-28, 2010-04-20, 2010-04-22, 2010-05-16, 2010-05-18, 2010-06-14, 2010-07-10, 2010-08-05, 2010-09-02, 2010-09-26, 2010-09-30, 2010-10-25, 2010-11-17, 2010-11-21, 2010-12-16	18	22416
2 Superorb. phase : 0.5 – 0.7 Orbital phase : 0.6 – 0.8	XRT	2006-09-05, 2006-11-21 - 2006-11-24, 2006-12-18, 2006-12-20, 2006-12-22, 2011-01-14, 2011-10-01	10	20147
	PCA	2006-10-27, 2006-10-29, 2011-01-09, 2011-01-13, 2011-02-06, 2011-02-09, 2011-03-06, 2011-03-31, 2011-04-03, 2011-04-28, 2011-05-22, 2011-05-26, 2011-06-19, 2011-07-13, 2011-07-17, 2011-08-10, 2011-08-14, 2011-09-07, 2011-10-03, 20011-10-30	20	24384
3 Superorb. phase : 0.0 – 0.2 Orbital phase : 0.0 – 0.2	XRT	2008-10-22, 2008-11-19, 2008-12-17, 2013-11-23, 2013-12-14, 2014-01-11	6	10266
	PCA	2008-10-22, 2008-10-25, 2008-11-17, 2008-11-19, 2008-12-13, 2008-12-17, 2009-01-10, 2009-02-04, 2009-02-07, 2009-03-05, 2009-03-29, 2009-04-02, 2009-04-26, 2009-05-21, 2009-05-25, 2009-06-18, 2009-07-12, 2009-07-15, 2009-08-08	21	32912

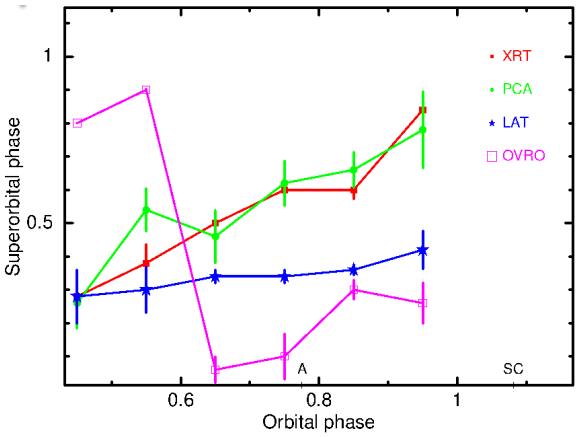

Fig. 3.— Superorbital phase at peak flux from fitted sinusoidal function given in Table 1 as a function of orbital phase bins for XRT, PCA, Fermi-LAT and OVRO data. Positions for apastron (A) and superior conjunction (SC) are marked.

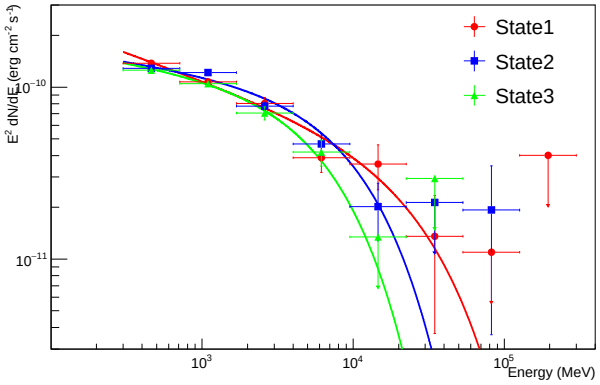

Fig. 4.— A cutoff power law fit to Fermi-LAT data for the three different states. Best-fit curves are shown as solid lines.

TABLE 3
Best-fit parameters of a power-law (with absorption) fit to the data for XRT and PCA

	Only XRT		
	N_H (10^{22} cm^{-2})	alpha	norm
state1	0.68±0.05	1.58±0.06	$(2.51\pm0.21)\times10^{-3}$
state2	0.70±0.05	1.53±0.05	$(3.08\pm0.20)\times10^{-3}$
state3	0.69±0.11	1.47±0.12	$(1.25\pm0.20)\times10^{-3}$
	XRT+PCA (all layers)		
	N_H (10^{22} cm^{-2})	alpha	norm
state1	0.81±0.04	1.79±0.03	$(3.22\pm0.15)\times10^{-3}$
state2	0.90±0.03	1.78±0.03	$(4.27\pm0.17)\times10^{-3}$
state3	1.05±0.08	1.95±0.05	$(2.25\pm0.18)\times10^{-3}$

TABLE 4
Parameters of a cutoff power law fit to the Fermi-LAT data for three different states

parameters	state1	state2	state3
α	2.31	2.12	2.12
flux	2.48×10^{-7}	2.41×10^{-7}	2.28×10^{-7}
Ec (MeV)	30041	10000	6338
TS	2663	2727	2328

from accretion disk or companion star in addition to the SSC component. Radiation density (U_{rad}) is estimated from luminosity L using expression $U_{rad} = L/4\pi R^2 c$, where R is the distance of the emission volume from the companion star or the accretion disk. Radiation density from the companion star, with $L_c = 2\times10^{38}$ erg s^{-1} and a distance of $R \sim 10^{12}$ cm, is about 4 orders of magnitude higher than the corresponding radiation density from the accretion disk. Hence, we have considered only the seed photons from the companion star for the External Compton model. However, this spectrum can-

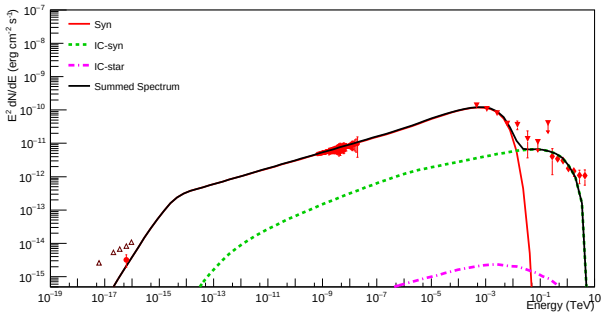

FIG. 5.— The SED of LS I +61°303 for state1. The synchrotron and inverse Compton spectra are calculated using the parameters as given in Table 5. X-ray, Fermi-LAT and VERITAS data for state 1 are shown with points in red color. Radio data shown in the figure do not correspond to state 1. The average flux from OVRO is shown with filled circle of red color, whereas radio data from Strickman et al. (1998) is shown with brown triangles.

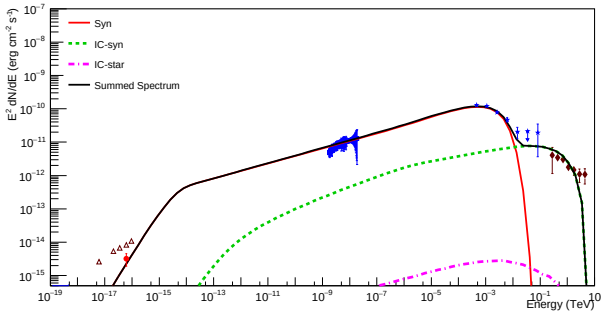

FIG. 6.— The SED of LS I +61°303 for state2. The synchrotron and inverse Compton spectra are calculated using the same parameters as given in Table 5. X-ray and Fermi-LAT data for state 2 are shown with points in blue color. Since, VERITAS data for state 2 is not available, state 1 VERITAS data is used which is shown in brown colour. Radio data are the same as in Fig. 5.

not explain the observed data as seen from Figure 5 and Figure 6. In this case, we have considered radius of the emission volume as a parameter for the fit to the data. We can also estimate the radius of emission volume from the variability time scale of the source. We fixed the size of the emission region according to the estimates from variability study (Smith et al. 2009), which indicates a possible size of the emission region to be $\sim 6 \times 10^{10}$ cm. Considering that the bulk Lorentz factor is 1.25, this size corresponds to $\sim\ 7.5 \times 10^{10}$ cm. Fixing the emission region size to this value, model parameters were estimated which are given in the last column of Table 5. Although the synchrotron spectrum explains the observed fluxes from radio to MeV–GeV energies, SSC spectrum alone cannot fit the data well. Hence we have also estimated the contribution of companion star photons for this low magnetic field case and we found that the external Compton model overestimates the observed flux at MeV–TeV energies. However, SSC and EC models together can explain the data well if the companion star luminosity is considered to be reduced by a factor of 10. This is shown in Figure 7.

In the spectral fitting, we did not consider the radio data (triangles in Fig. 6, 5 and 7) from VLA observation (Strickman et al. 1998) in fit, since the orbital and superorbital phases for these are different from the phases

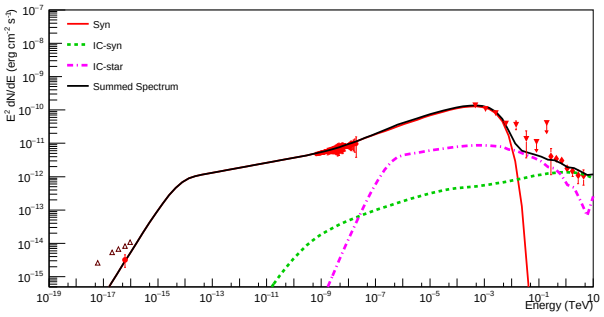

FIG. 7.— The SED of LS I +61°303 for state1. The synchrotron and inverse Compton spectra are calculated using the same parameters given in the last column of Table 5, with the emission region radius decided from the variability time scale.

TABLE 5
PARAMETERS OF THE FIT FOR MICROQUASAR SCENARIO

Parameters	state1	state2	state1 (radius from variability study)
Magnetic field (Gauss)	5×10^3	5×10^3	15
γ_{min}	4.4	4.9	110
γ_{max}	5.6×10^6	5.4×10^6	9.0×10^7
spectral index (α)	2.53	2.55	2.7
spectral index (β)	2.34	2.40	2.4
radius (cm)	11.5×10^7	18.0×10^7	7.5×10^{10}
Gamma Break	1.0×10^5	1.4×10^7	9.0×10^4
Bulk Lorentz factor	1.25	1.25	1.25
Distance (kpc)	2.0	2.0	2.0
Inclination angle(deg)	30.0	30.0	30.0
Luminosity (erg/s)	3.9×10^{35}	3.8×10^{35}	4.3×10^{35}

for state 1 and state 2. Since, the energy spectrum is not available for OVRO data, we have used average flux as an upper-limit for SED modelling, and for the chosen set of parameters the model does not overestimate radio fluxes for the states considered above.

5. DISCUSSION AND CONCLUSIONS

Long-term timing analyses of LS I +61°303 at different wavelengths has shown some of the interesting characteristics of the source. Flux in various wavebands shows variation with superorbital phase and this variation is wavelength dependent as well as the binary phase dependent. At X-ray energies, as evident from Figure 1, the source is bright at orbital phases $\sim 0.4 - 0.8$ and superorbital phases of $\sim 0.3 - 0.8$. Whereas at radio energies, the source is bright at orbital phases of $\sim 0.4 - 0.8$ and superorbital phases of $\sim 0.7 - 1.4$. The γ-ray flux in MeV-GeV band as given by Fermi-LAT shows a shift relative to the radio and the X-ray bands. This behaviour possibly indicates that radio, X-ray and γ-ray emissions could be originating from different regions.

The long-term superorbital modulation of flux could support the scenario where circumstellar disk of a Be star quasi-cyclically expands and shrinks (e.g., Negueruela et al. (2001)). However, for such a scenario the long-term period is variable from cycle to cycle (Rivinius et al. 2013). Recent analysis of radio data established the fact that the long-term period is quite stable over 8 cycles (Massi & Torricelli-Ciamponi

2016) which makes the scenario of quasi-cyclic variation of circumstellar disk of the Be star for LS I +61°303 less probable. This stable superobital modulation is attributed to periodic Doppler boosting effects of the precessional jets associated with the compact objects (Massi & Torricelli-Ciamponi 2014).

In this paper, we have seen that the modulation of flux with superorbital phase is more prominent in orbital phase bins near apastron. This is clearly seen at various wavelengths in Figures 2 and 3. Although the long-term superorbital variation does not support the variation of circumstellar disk size, this type of superorbital modulation near the apastron could stem from the interaction of the compact object with the circumstellar disk of the Be star. The equivalent width (EW) of the Hα emission line is related to the size of the stellar disk (Zamanov & Martí 2000; Grundstrom et al. 2007). In addition to that, it has been found that the maximum of the EW of Hα occurs in a region around superorbital phase of $\sim$ 0.4 (see Zamanov et al. (1999); Zamanov & Martí (2000)) considering superorbital period of 1584 days. However, if we use superorbital period as 1626 days then the maximum of the EW of Hα occurs at $\sim$ 0.3. From Figure 3 we see that flux of gamma-rays is high at the superorbital phase of $\sim$ 0.3–0.5, which suggests that the disk plays an important role in modulating γ-rays. Although, a similar enhancement of X-rays at superorbital phase of 0.2 is seen by Li et al. (2011) considering only peak flux, we see that X-ray flux peaks at the superorbital phases in the range of $\sim$ 0.4–0.8 depending on the orbital phase. We see that the peak of radio flux is shifted further. It suggests that even if the disk size plays a significant role for γ-rays, X-ray and radio fluxes are not necessarily affected much by the size of the disk.

Figure 2 shows that, for all wavebands, the superorbital variability is not significant in the periastron region, whereas it is significant at the apastron. This can support the scenario where one assumes that the interaction between compact object and the circumstellar disk of Be star is strong when compact object is in the proximity of Be star. As a result, superorbital modulation effect becomes insignificant as suggested by Ackermann et al. (2013). However, it becomes dominant as the compact object starts moving towards the apastron region.

Another possible scenario for the modulation is related to the precession of the Be star disk about the orbital plane. If this scenario is adopted for possible explanation of the strong superorbital modulation in the apastron phase, then the angular distance between orbital plane and the disk plane should become minimum. As a result, even if the compact object is far from the Be star, the smaller angular distance between disk plane and orbital plane provides relatively higher interaction of the compact object with the disk.

In addition to the superorbital modulation in the apastron phase (0.5 – 1.0) we have seen phase lag among radio, X-ray and γ-rays. The possible explanation for the constant phase lag between X-ray and radio is that the plasma blobs filled with high-energy particles may escape from the X-ray emission region to the radio emission region which is at a distance of $\sim$ 10 times the binary separation distance as proposed by Chernyakova et al. (2012) in the context of pulsar wind scenario. However, in the microquasar scenario, different regions in the jets can be responsible for the phase lag. We have also seen the phase lag between radio and γ-rays. In such binary systems, γ-rays are considered to be produced by up-scattering of radio photons or accretion disk/star photons. If the γ-rays are originating through the up-scattering of radio photons which are being produced by the same population of electrons then there should not be any phase lag between radio and γ-rays. Hence, up-scattering of a separate population of photons could be a possible explanation for the phase lag between γ-ray and radio fluxes.

In addition to the timing analysis, we also tried to understand the spectral behaviour of the source at different orbital and superorbital phases. We have chosen three different regions following flux variations for X-ray, radio, and γ-rays as function of orbital and superorbital phase. From Figure 1 we see that the source at high energy is mostly very active in the orbital phase bin of 0.5–0.8 and superorbital phase bin 0.3–0.7. We selected two different regions with superorbital phase 0.3–0.5; orbital phase: 0.6–0.8 (state1) and superorbital phase: 0.5 – 0.7; orbital phase: 0.6 – 0.8 (state2) from this region where source is bright at all wavelengths. To compare the spectral variation with the other orbital and superorbital phases where the source is not bright, we have chosen a region with superorbital phase 0.0 – 0.2 and orbital phase 0.0 – 0.2 (state3). Based on these three different regions of orbital or superorbital phases, we have analysed X-ray and Fermi-LAT data to see the spectral behaviour of the source at high energies. We found no significant differences between flux levels but we see some variations in the spectral indices at Fermi-LAT energies. However, we see some difference in both the spectral indices and flux levels for XRT-PCA data, though the interplay of the spectral shape and the absorption playing a role in this trend cannot be ruled out.

From the fit to the SED we have seen that we can explain the data well considering LS I +61°303 as a microquasar. In the microquasar model, it is generally assumed that the high energy emission comes from the region which is very close to the compact object to reduce the effect of $\gamma\gamma$ absorption due to radiation field of companion star (Gupta et al. 2006). Magnetic field in this region is relatively high as considered for our model, and we have estimated emission volume of the order of 10^8 cm. In this emission volume, some the of the emitted γ-rays can be absorbed through e^+e^- pair creation process due to X-ray photons in emission volume. We have estimated that about 20% of γ-rays will be absorbed at TeV energies. However, larger sizes of emission volume will make this absorption insignificant. We have seen that it is possible to have lower values of magnetic field strength to explain the observed data, in case of larger emission volume.

We have also seen in section 4 that if we consider the radius of emission volume obtained from variability study, the magnetic field from the model fit to the data is estimated to be $\sim$ 10 G. However, we found that the SSC model alone cannot explain the TeV data well and EC model overestimates the observed flux for the luminosity of the companion star $\sim$ 10^{38} erg s^{-1}. A lower value of this luminosity ($\sim$ 10^{37} erg s^{-1}) can explain the data well. This suggests that lower values of magnetic field in the emission blobs are suitable for LS I +61°303 to

explain the observed data constraining the luminosity of the companion star. With high magnetic field, the Synchrotron cooling timescale is much smaller than the variability timescale which could be as low as 2 seconds as estimated by Smith et al. (2009). In our SED fitting, we have considered that the emitting blob is close to the compact object. The blob size increases as it moves away from the compact object in the jets and magnetic field reduces. The time-averaged values of flux from a particular region in the jet as considered by Gupta et al. (2006) could reduce the discrepancy between Synchrotron cooling time scale and the time scale of X-ray flux variability. From the SED, it seems that the one single emission process is responsible for X-ray and MeV-GeV data. Hence, we have considered Synchrotron emission process to explain the data up to GeV energies. As a result, a high magnetic field is required to explain the data if the maximum energy of high energy electrons is not well above $\sim$ 1 TeV. A good quality data in the hard X-ray region can establish whether a different emission component is required to explain the data at MeV-GeV region. It can also indicate if we need a different population of electrons to explain data at different energy bands in the SED.

We have also seen that the fitted model parameters show hardening of spectral index after break (see Table 5). In addition, flux levels for different states (mainly X-ray) are different. A change in the location of the compact object relative to the companion star during the orbital and the superorbital cycles and its interaction with circumstellar disk could be responsible for the changing electron spectral distribution.

In the context of timing analysis, we have seen the phase lag among radio, X-ray and γ-ray data which may suggest that they originate from different emission regions. However, in our present spectral modelling we have considered single emission zone to explain the mutiwavelength data. To support the scenario of different origins we need simultaneous multiwavelength data for longer period both for timing and spectral analysis. At present, we have such observation for radio, X-ray and MeV–GeV gamma-rays. However, GeV–TeV data is also required to get a complete understanding of the source in multifrequencies.

The following major conclusions can be drawn, based on the study presented here:

- The super orbital modulation is more pronounced near the apastron for all wavelengths, supporting geometric scenarios as a cause for the super orbital modulation.
- There is a definite wavelength dependent variation of the maximum of the super orbital flux with respect to the binary phase. This variation shows a wavelength dependent shift.
- Emission from radio to GeV gamma-rays during the maximum emission can be modelled by an one-zone micro-quasar jet model. To explain the TeV emission, Comptonization from an External Compton source is necessary especially when low magnetic field is assumed. In this case, we suggest that the photons from the companion star, with a lower luminosity ($\sim 10^{37}$ erg s^{-1}), is adequate to explain the data.
- Extended hard X-ray data would be necessary to constrain the synchrotron model and TeV observations across a super orbital cycle, along with X-ray measurements, would be required to make a detailed emission model for this source.

ACKNOWLEDGEMENTS

We acknowledge the use of data from the High Energy Astrophysics Science Archive Research Center (HEASARC), provided by NASA's Goddard Space Flight Center. Also the data supplied by the UK Swift Science Data Centre at the University of Leicester has been used in present work. We thank Hovatta Talvikki for providing us data from OVRO 40-m monitoring program which was used in the research by (Richards et al. 2011)(supported in part by NASA grants NNX08AW31G and NNX11A043G, and NSF grants AST-0808050 and AST-1109911). We acknowledge the use of Fermi-LAT data and analysis tool from Fermi Science Support Center. We would also like to thank MAGIC collaboration for making their published data public which has been used in this work. We also acknowledge VERITAS collaboration for their published data used in this work.

REFERENCES

Abdo, A. A., Ackermann, M., Ajello, M., et al. 2009, ApJS, 183, 46
Acciari, V. A., Aliu, E., Arlen, T., Aune, T., et al. 2011, ApJ, 738, 3
Acciari, V. A., Beilicke, M., Blaylock, G., et al. 2008, ApJ, 679, 1427
Ackermann, M., Ajello, M., Ballet, J., et al. 2013, ApJL, 773, L35
Albert, J., Aliu, E., Anderhub, H., et al. 2009, ApJ, 693, 303
—. 2006, Sci, 312, 1771
Aleksic, J., Alvarez, E. A., Antonelli, L. A., et al. 2012, ApJ, 746, 80
Aliu, E., Archambault, S., Behera, B., et al. 2013, ApJ, 779, 88
Aragona, C., McSwain, M. V., Grundstrom, E. D., et al. 2009, ApJ, 698, 514
Atwood, W. B., Abdo, A. A., Ackermann, M., et al. 2009, ApJ, 697, 1071
Bradt, H. V., Rothschild, R. E., & Swank, J. H. 1993, A$AS, 97, 355
Burrows, D. N., Hill, J. E., Nousek, J. A., et al. 2005, SSRv, 120, 165
Chernyakova, M., Neronov, A., Molkov, S., et al. 2012, ApJL, 747, L29
Dhawan, V., Mioduszewski, A., & Rupen, M. 2006, in Proc. of Microquasars and Beyond: From Binaries to Galaxies, Vol. 52,
Evans, P. A., Beardmore, A. P., Page, K. L., et al. 2007, A&A, 469, 379
Frail, D. A., & Hjellming, R. M. 1991, AJ, 101, 2126
Gregory, P. C. 2002, ApJ, 575, 427
Grundstrom, E. D., Caballero-Nieves, S. M., Gies, D. R., et al. 2007, ApJ, 656, 431
Gupta, S., & Bottcher, M. 2006, ApJL, 650, L123
Gupta, S., Böttcher, M., & Dermer, C. D. 2006, ApJ, 644, 409
Hutchings, J. B., & Crampton, D. 1981, PASP, 93, 486
Li, J., Torres, D. F., Zhang, S., et al. 2012, ApJL, 744, L13
—. 2011, ApJ, 733, 89
Massi, M., & Jaron, F. 2013, A&A, 554, A105
Massi, M., Jaron, F., & Hovatta, T. 2015, A&A, 575, L9
Massi, M., Ribó, M., Paredes, J. M., et al. 2004, A&A, 414, L1
Massi, M., Ros, E., & Zimmermann, L. 2012, A&A, 540, A142
Massi, M., & Torricelli-Ciamponi, G. 2014, A&A, 564, A23
—. 2016, A&A, 585, A123

Negueruela, I., Okazaki, A. T., Fabregat, J., et al. 2001, A&A, 369, 117
Paredes, J. M., Massi, M., Estalella, R., & Peracaula, M. 1998, A&A, 335, 539
Richards, J. L., Max-Moerbeck, W., Pavlidou, V., et al. 2011, ApJS, 194, 29
Rivinius, T., Carciofi, A. C., & Martayan, C. 2013, A&A Rev., 21, 69
Sanchez, D. A., & Deil, C. 2013, ArXiv e-prints, arXiv:1307.4534
Smith, A., Kaaret, P., Holder, J., et al. 2009, ApJ, 693, 1621
Strickman, M. S., Tavani, M., Coe, M. J., et al. 1998, The Astrophysical Journal, 497, 419
Zamanov, R., & Martí, J. 2000, A&A, 358, L55
Zamanov, R. K., Martí, J., Paredes, J. M., et al. 1999, A&A, 351, 543